UC Davis

UC Davis Previously Published Works

Title

Superior tensile creep behavior of a novel oxide dispersion strengthened CrCoNi multi-principal element alloy

Permalink

https://escholarship.org/uc/item/5jn8g64j

Authors

Sahragard-Monfared, Gianmarco

Zhang, Mingwei

Smith, Timothy M

et al.
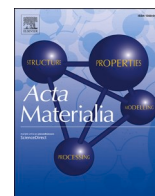
Superior tensile creep behavior of a novel oxide dispersion strengthened CrCoNi multi-principal element alloy

Gianmarco Sahragard-Monfared [a], Mingwei Zhang [b,c], Timothy M. Smith [d], Andrew M. Minor [b,c], Jeffery C. Gibeling [a,*]

[a] Department of Materials Science and Engineering, University of California, One Shields Avenue, Davis, CA 95616
[b] National Center for Electron Microscopy, Molecular Foundry, Lawrence Berkeley National Laboratory, 1 Cyclotron Road, Berkeley, California 94720
[c] Department of Materials Science and Engineering, University of California, 2607 Hearst Avenue, Berkeley, California 94720
[d] High Temperature and Smart Alloys Branch, NASA Glenn Research Center, 21000 Brookpark Rd., Cleveland, Ohio 44135

ARTICLE INFO

ABSTRACT

The creep behavior of an additively manufactured (AM) yttrium oxide dispersion strengthened (ODS) CrCoNi multi-principal element alloy (MPEA) is investigated in this study. Tests were conducted over a constant tensile stress range of 40–200 MPa and a temperature range of 973–1173 K. A stress exponent of 6.5 ± 0.1 and activation energies in the range of 335–367 kJ/mol were measured. Compared to its non-ODS counterpart and its parent alloy (CrMnFeCoNi), AM ODS CrCoNi has superior creep resistance at all tested stresses and temperatures. The mechanism contributing to the excellent creep resistance of AM ODS CrCoNi is attributed to the interaction of mixed character dislocations with oxide particles. The creep ductility of AM ODS CrCoNi is higher than its non-ODS counterpart due to a large percentage of low angle grain boundaries associated with its columnar grain structure. It was also found that creep ductility is significantly greater at the highest applied stress of 200 MPa compared to lower stresses. The steady state dislocation structure of AM ODS CrCoNi consists of long arrays of dislocations, which is different from that observed in non-ODS CrCoNi which consists of individual curved dislocations.

1. Introduction

Multi-principal element alloys (MPEA), often referred to as high entropy alloys or compositionally complex alloys, are materials in which high proportions of three to five elements are present, typically with a minimum threshold of 10 at% of each element. FCC MPEAs such as equiatomic CrMnFeCoNi (Cantor alloy) and a ternary derivative, CrCoNi, have been studied extensively and exhibit excellent strength and ductility at cryogenic and room temperatures [1–4]. Of the Cantor alloy derivatives, CrMnCoNi has the highest yield strength while the Cantor alloy itself achieves the highest ductility, although CrCoNi generally displays the best combination of strength, ductility, and damage tolerance [5,6]. The formation of nanotwin-HCP lamellae in CrCoNi at moderate temperatures partitions grains into much smaller structural units that can sustain large lattice rotations, which contributes to extensive strain hardening and to which the superb combination of properties in this material is ascribed [4]. However, poor strength at elevated temperatures has limited the range of applications of MPEAs in

areas such as gas turbine engines and thermal energy conversion systems [7,8].

To overcome this limitation, several investigators have added Ti, Al, and other elements to enhance high temperature strength and other material properties of MPEAs and have essentially created high entropy superalloys [9–13]. However, the addition of these elements alters the MPEA matrix and thus does not take advantage of its unique attributes. Other investigators have used oxide dispersion strengthening (ODS) to increase the high temperature strength and compression creep resistance of MPEAs. For example, Hadraba, et al. added O_2 gas, Y, and Ti to a blend of pure Cantor alloy powders during mechanical alloying with subsequent spark plasma sintering (SPS) of the alloyed powders [14]. Through this process, they demonstrated that it is possible to retain the MPEA matrix with the addition of dispersoids that interact with low angle dislocation boundaries and individual dislocations to improve creep resistance [15]. Smith, et al. have also successfully manufactured an ODS MPEA by laser powder bed fusion (L-PBF) of acoustically mixed yttria-coated CrCoNi particles followed by a hot isostatic pressing (HIP)

---

* Corresponding author at: Jeffery C. Gibeling, Department of Materials Science and Engineering, University of California, One Shields Avenue, Davis, CA 95616.
  E-mail address: jcgibeling@ucdavis.edu (J.C. Gibeling).

cycle to cost effectively create additively manufactured (AM) ODS CrCoNi with minimal residual stress [16]. The addition of yttria to the CrCoNi matrix significantly increased the room and high temperature tensile strength of this alloy after HIPing.

Materials manufactured via different processing methods commonly have dissimilar mechanical properties. Substantial differences in microstructure, mechanical properties, and strengthening mechanisms were found by Yang, et al. for an FeCrNiAl medium entropy alloy fabricated by vacuum arc melting, SPS, and hot-press sintering [17]. Sahragard-Monfared, et al. investigated the effect of processing methods on tensile creep properties of wrought and additive manufacturing (AM) CrCoNi and found the latter exhibited higher creep resistance and lower creep ductility than the former. This difference was attributed to the higher volume fraction of Cr-rich oxides and fewer low angle grain boundaries (LAGB) in the AM material. It was also found that the CrCoNi MPEA in both the wrought and AM forms exhibited superior creep resistance compared to the wrought Cantor alloy [8]. With the advancement of AM as a novel, economically viable method for introducing dispersoids into a metal matrix, the new feasibility of ODS makes it an excellent option for overcoming the high temperature strength limitations of FCC MPEAs. Although the elevated temperature strength of BCC MPEAs is currently of great interest, the superior oxidation resistance of FCC MPEAs makes them more suitable for certain applications without requiring high temperature coatings [18–20]. Additionally, the tensile ductility of FCC MPEAs is significantly greater than that of BCC MPEAs [21]. In order to more fully explore the opportunities afforded by the addition of ceramic dispersoids, this study focuses on the creep properties of AM ODS CrCoNi produced by additive manufacturing.

2. Experimental methods

The AM ODS CrCoNi was fabricated by L-PBF of acoustically mixed pre-alloyed equiatomic CrCoNi and 1 wt% of Y_2O_3 powder with a diameter sizes ranging between 10–45 µm and 100–200 nm, respectively, as described by Smith, et al. [16]. However, even though 1 wt% of oxide was used to coat the powder, the volume fraction of yttria in the final material is 0.6 vol% [16]. Two blanks of AM ODS CrCoNi with a geometry of 88.9 (L) x 15.875 (W) x 15.875 (T) mm were fabricated as a single build and then HIPed at 1458 K to relieve residual stress and densify the material, resulting in 99.9% dense builds. The use of acoustic mixing as opposed to mechanical alloying processes such as high energy ball milling was chosen to ensure the powders did not deform and retained flow properties amenable to AM. A secondary benefit of this approach is its lower cost compared to conventional mechanical alloying processes [16]. Specimens were electrical discharge machined from the build such that their creep tensile axis (Z-direction) is parallel to the build direction. Fig. 1 illustrates an isometric view of a tensile creep specimen with gage section dimensions of 35.56 (L) x 2.54(W) x 1.00(T) mm. The surfaces and edges of the gage sections of each specimen were polished using 600 grit SiC paper to minimize the risk of surface defects influencing creep properties.

Scanning electron microscopy (SEM) was performed on a Thermo Fisher Quattro S ESEM and an FEI Scios Dual Beam FIB/SEM equipped with EDS and EBSD detectors. All microscopy samples were prepared by grinding and polishing to 0.3 µm with an alumina suspension and then vibropolishing with 0.05 µm colloidal silica for 4 h. The Quattro ESEM was used in backscatter electron mode to characterize the fractured specimens. The Scios FIB/SEM was used to characterize atomic composition via energy dispersive x-ray spectroscopy (EDS) and the grain orientations and boundary misorientations via electron back-scatter diffraction (EBSD). EDS was performed at an operating voltage of 30 kV and EBSD was performed at an operating voltage of 15 kV and step size of 0.8 µm. The EBSD data were post-processed with MTEX (version 5.7.0) in MATLAB following a procedure similar to that employed of Broyles, et al. such that unreasonably small grains are removed and unindexed data points are filled based on the orientations of their neighbors [22]. The processed EBSD data were used to calculate a grain average Taylor factor. Average grain size was determined from the boundary misorientation maps using the line intercept method.

Diffraction contrast imaging (DCI)-STEM was performed on an FEI monochromated F20 UT Tecnai S/TEM at an accelerating voltage of 200 kV to observe the dislocation structure of HIPed, annealed, and crept specimens and to determine the character of dislocations interacting with particles through $g \bullet b$ analyses. STEM-EDS was carried out on an FEI TitanX 60–300 at an accelerating voltage of 300 kV to identify the composition of particles. TEM specimens from creep samples before deformation and interrupted at steady state deformation were prepared by grinding and polishing the specimen gage surface to 1200 grit and less than 100 µm thickness. The TEM samples were then twin-jet electropolished at −20 °C using a Fischione Model 110 Automatic Twin-Jet Electropolisher in a 70% methanol, 20% glycerol, and 10% perchloric acid solution.

Constant stress tensile creep tests were performed under vacuum ($\leq 3 \times 10^{-5}$ torr) to avoid oxidation, following the procedures described in previous studies [8,23]. Tests were performed in the ranges of 1023–1173 K (0.6–0.7 T_m) and 40–200 MPa and were conducted until fracture to clearly identify the steady state creep rate except for those
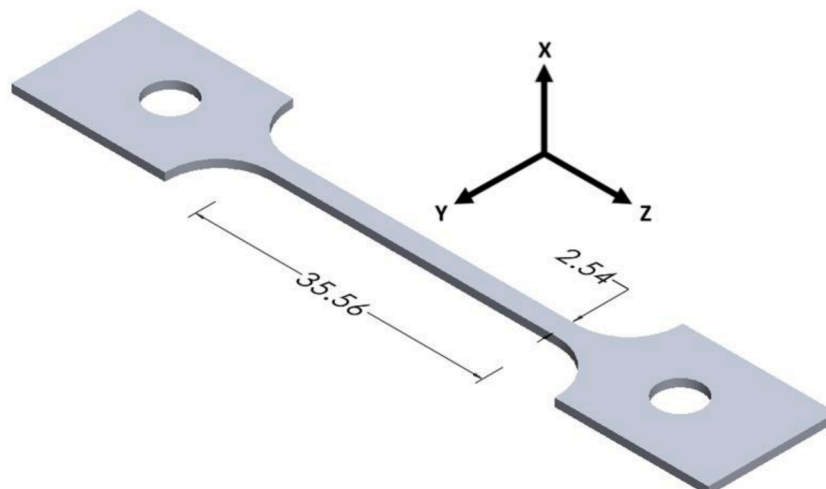

Fig. 1. Isometric view of a creep specimen. All dimensions are in mm.

terminated after steady state for TEM observation. The dislocation structure of those samples was preserved by furnace cooling the specimen under the same creep load.

3. Results and discussion

3.1. Characterization of initial microstructure

Although a uniform distribution of elements has previously been observed in AM CrCoNi, it is important to examine the distribution of elements in this ODS material to confirm this uniformity after the addition of yttria [8,24,25]. Fig. S1 illustrates the initial chemical composition of AM ODS CrCoNi as determined by SEM-EDS and shows an equiatomic composition with a uniform distribution of the three principal elements. Yttrium and oxygen are not included in Fig. S1 due to resolution limitations of the FEI Scios Dual Beam FIB/SEM and the small amount of yttria. However, Smith, et al. have demonstrated that the yttria is well distributed in the microstructure of this material [16].

The EBSD inverse pole figure (IPF) color maps and contour plots displayed in Fig. 2 illustrate that there is slight texture favorable to the [111] direction in the YZ plane and the [001] direction in the XZ plane, although the XY plane shows no texture. However, the intensities of these observed textures are low at a maximum value of three for the YZ

plane while heavily textured materials exhibit much higher values. Additionally, the calculated Taylor factors for each of these EBSD maps are within 4% of each other (Table 1) and thus the texture observed is not expected to significantly affect the creep properties of AM ODS CrCoNi. As noted by Smith, et al., the formation of annealing twins was suppressed in this material, which is unusual for CrCoNi [8,16,26,27]. The lack of twin boundaries (TB) in AM ODS CrCoNi compared to its wrought and non-ODS counterparts is likely due to the pinning of grain boundaries (GB) by the yttria particles, which suppresses recrystallization.

Figure 3 shows boundary misorientation plots of the XY and YZ planes of AM ODS CrCoNi from which grain sizes were determined. The AM ODS CrCoNi grains are elongated in the build direction with an aspect ratio of approximately 4:1 such that the grain size is 23.8 ± 1.8 μm in the Z-direction of the YZ plane and 6.5 ± 1.8 μm in the Y-direction of the YZ plane. As noted by Smith, et al., the yttria suppressed recrystallization and grain growth during the L-PBF build process and subsequent HIP cycle by pinning the grain boundaries. Fig. 3 illustrates the large percentage of LAGBs in the AM ODS CrCoNi; the distributions of misorientation angles for the YZ and XY planes are plotted on histograms in Fig. S2. Table 1 lists important quantitative descriptors of the microstructures of the materials studied in this investigation (wrought, AM, and AM ODS CrCoNi), including the percentages of the different
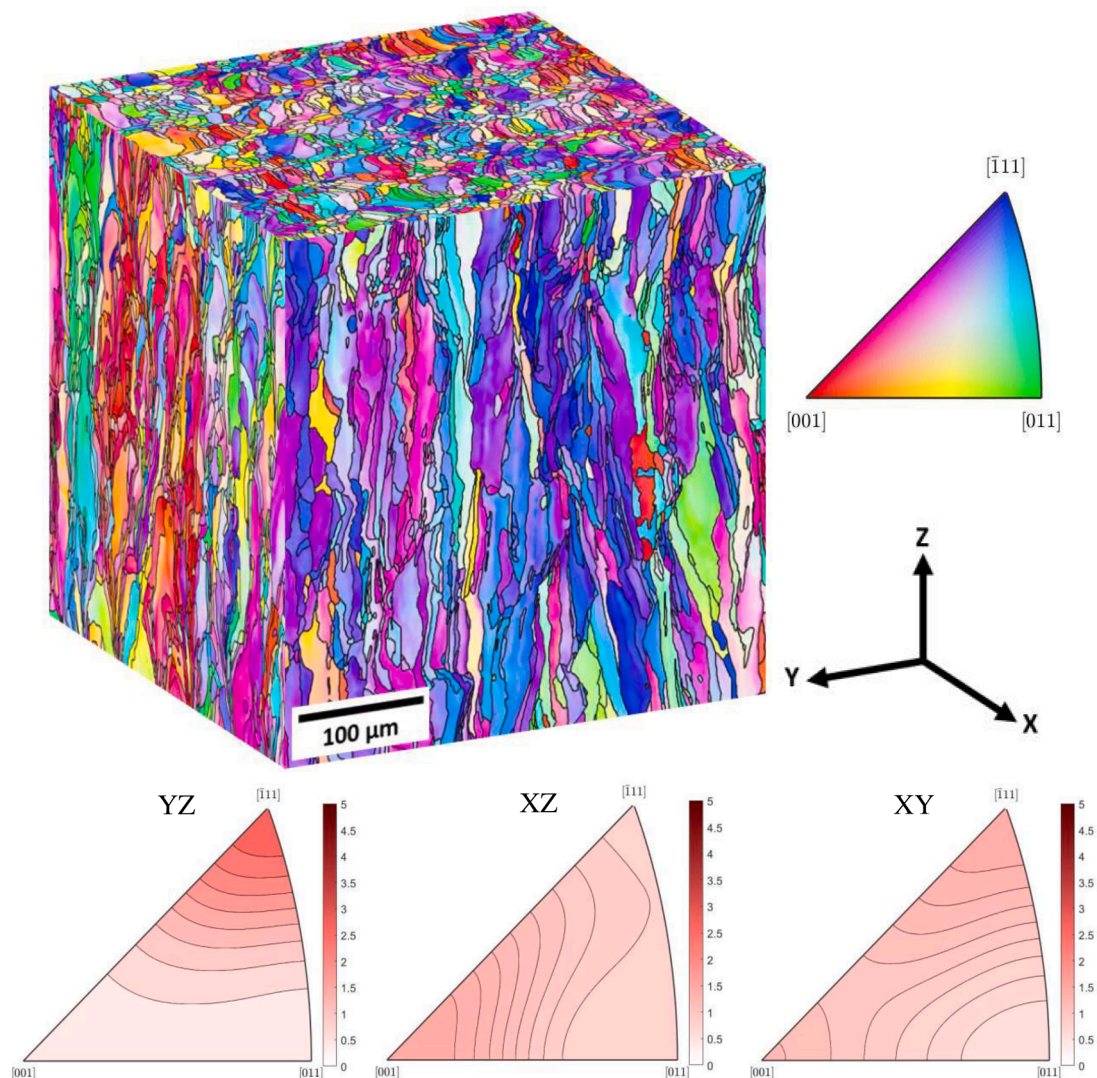

Fig. 2. EBSD-IPF color cube and IPF contour plots of AM ODS CrCoNi.

Table 1

Percentages of Low Angle Grain Boundaries, High Angle Grain Boundaries and Twin Boundaries.

Material	Grain Size Z-direction (μm)	Grain Aspect Ratio	Vol% Oxides	Taylor Factor	LAGB	HAGB	TB
AM ODS CrCoNi (YZ)	23.8 ± 1.8	4:1	1.2%	3.39	57.6%	38.8%	3.6%
AM CrCoNi (YZ)	74.3 ± 2.6	1.8:1	0.6%	3.27	0.9%	25.8%	73.3%
Wrought CrCoNi	31.2 ± 1.9	∼ 1:1	∼ 0%	3.32	3.2%	41.9%	54.9%
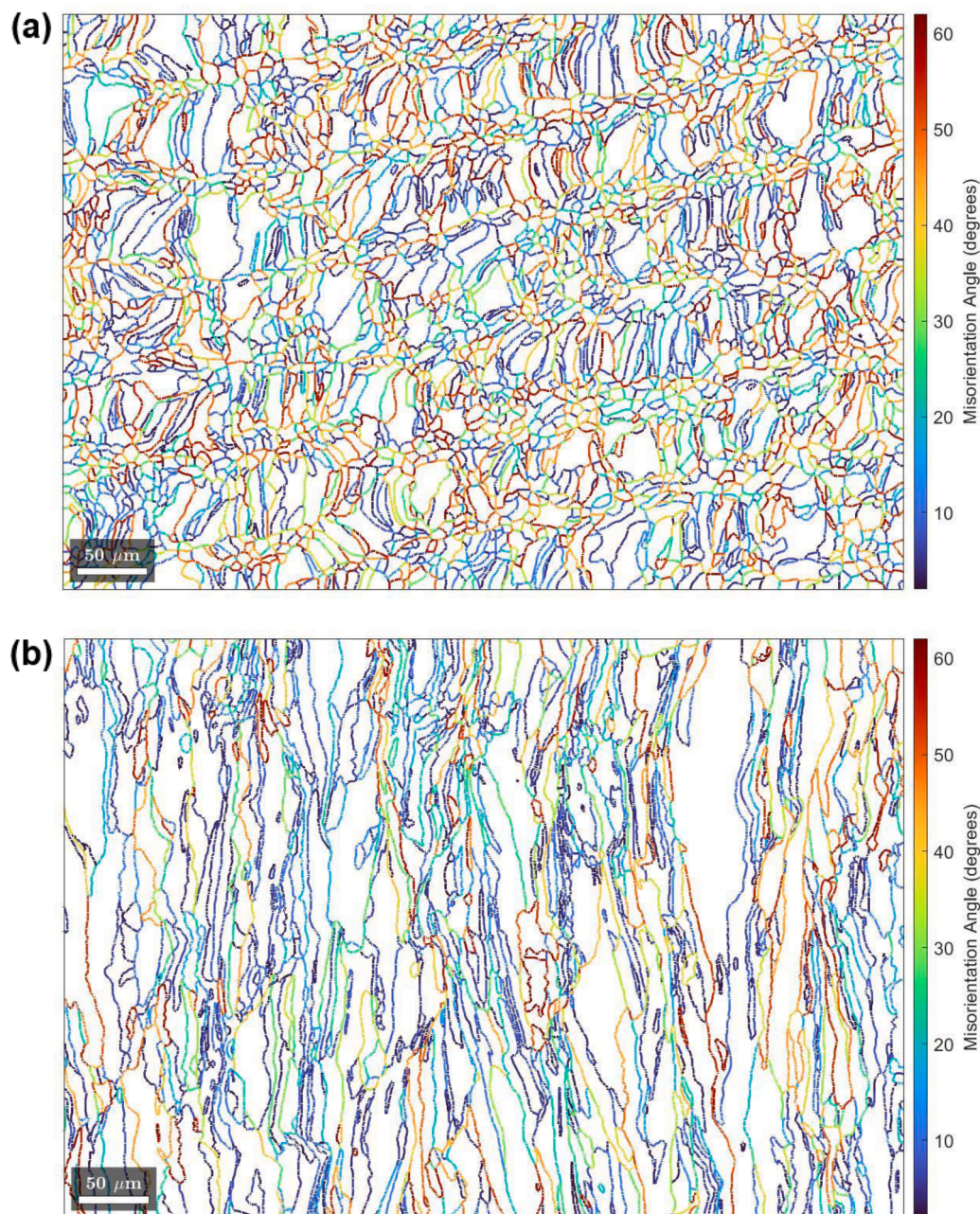
Fig. 3. Boundary misorientation plots of (a) XY plane (b) YZ plane of AM ODS CrCoNi.

types of boundaries. LAGBs, high angle grain boundaries (HAGB), and TBs are defined as follows: 1–15° (LAGBs), greater than 15° excluding TBs (HAGBs), and 60 ± 3° (TBs).

3.2. Creep results

Creep curves for representative temperatures and applied stresses are presented in Fig. 4, illustrating the effects of these testing conditions.

The AM ODS CrCoNi exhibits creep behavior typical of pure metals and alloys that behave like pure metals with distinct normal primary, secondary, and tertiary regions. However, the tertiary regime is significantly shorter in AM ODS CrCoNi compared to its non-ODS counterpart, indicating a rapid failure after cracks have formed [8]. Additionally, it is noted that the creep ductility is substantially higher at an applied stress of 200 MPa.

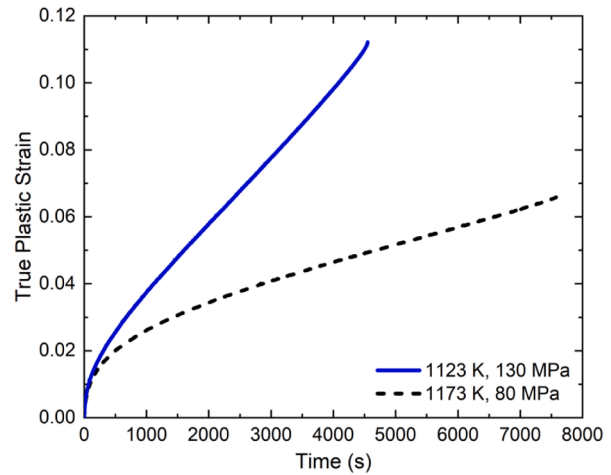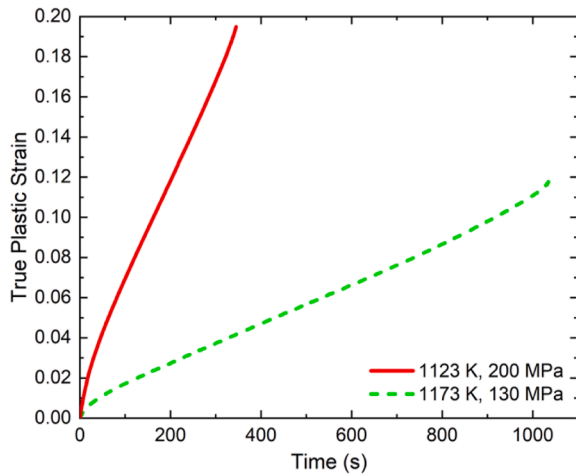Steady-state creep rates were calculated from the slopes of the sec-

Fig. 4. Representative creep curves of AM ODS CrCoNi.
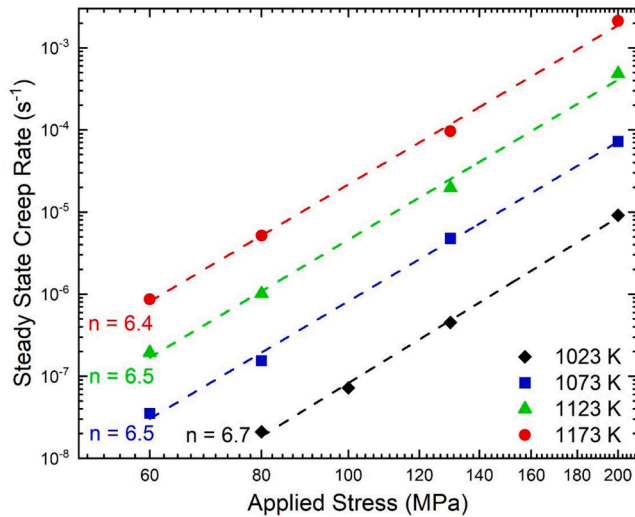

Fig. 5. Log-log plot of steady state creep rate vs applied stress for AM ODS CrCoNi.

ondary region of the creep curves and plotted as a function of applied stress to determine the stress exponents for each material; this relationship is shown on double logarithmic plots in Fig. 5. The power law equation (Eq. (1)) describes the relationship between steady state creep rate, $\dot{\varepsilon}_{SS}$, and applied stress, σ, where A is a material constant that includes dislocation structure, Q_C represents the creep activation energy, R is the gas constant, T is temperature, and n is the stress exponent [28].

$$\dot{\varepsilon}_{SS} = A\sigma^n \exp\left(-\frac{Q_C}{RT}\right) \tag{1}$$

An average stress exponent of 6.5 ± 0.1 was found for AM ODS CrCoNi. This value is slightly above the range commonly associated with the dislocation climb mechanism of creep deformation in subgrain forming metals and below the range for ODS alloys in which dislocation/particle interactions control the deformation. Stress exponents for ODS alloys typically range from 10 to 50, reaching as high as 75 for single crystal ODS alloys [29–31]. Although the alloy in this study is oxide dispersion strengthened, the inclusion of only 0.6 vol% yttria is likely too low to achieve high stress exponents classically associated with this strengthening method. However, this stress exponent is slightly higher than that of non-ODS AM CrCoNi (5.9 ± 0.1) revealing that the addition of yttria changes the stress dependence of the creep behavior [8]. The

stronger MPEA matrix compared to a pure matrix leads to synergistic control of dislocation motion by both the matrix and particles.

It is noted that strain rates at the highest stress and temperatures are essentially in the range of those measured in conventional tensile tests (1×10^{-3} s^{-1}). These test conditions were included to explore the possible onset of power law breakdown characterized by an increasing stress exponent with increasing stress (an upward curvature of the data in Fig. 5). However, the data remain linear on the double logarithmic plot and do not exhibit power law breakdown. Of equal importance, the data do not exhibit any tendency towards a threshold stress sometimes observed in ODS alloys at the lowest applied stresses.

To visualize the improved creep resistance of AM ODS CrCoNi compared to its non-ODS AM and wrought counterparts and wrought parent (Cantor) alloy, Fig. 6a illustrates a comparison of the steady-state creep rates and applied stresses of each of these alloys at a single temperature of 1023 K [7,8]. These data illustrate that AM ODS CrCoNi has better creep resistance than the other alloys. The stress exponent of the AM ODS CrCoNi is also higher than its non-ODS variants and the Cantor alloy when tested under similar conditions, implying different rate-controlling creep deformation mechanisms in these alloys. Fig. 6b illustrates a comparison of the constant stress tensile creep behavior of AM ODS CrCoNi from the present work to constant load compression creep behavior of SPS ODS Cantor alloy [15]. This comparison shows a significantly improved creep resistance in the AM ODS CrCoNi by three to four orders of magnitude.

The activation energy of AM ODS CrCoNi was determined from a semi-log plot of steady state creep rate versus 1/T as shown in Fig. 7. The values range from 335 to 367 kJ/mol for this material. The activation energy of non-ODS AM and wrought CrCoNi have been reported as being lower, ranging from 320 to 331 kJ/mol for AM and 240 to 259 kJ/mol for wrought, reflecting the increased temperature resistance provided by the AM process and the addition of yttria in the ODS material [8]. Additionally, the activation energy of the wrought Cantor alloy has been reported as 219–236 kJ/mol, again reflecting the better creep resistance of its derivative alloy [7].

The AM process and addition of oxides also affects the distribution of grain boundary misorientations which have an effect on creep resistance. For a LAGB, grain orientations on each side of the boundary are similar such that a lower stress concentration is required for the propagation of deformation to occur between these grains than those with a HAGB [32,33]. One contributing factor to the lower creep resistance of wrought CrCoNi compared to the AM version is reported to be a smaller percentage of LAGB in the AM material [8]. Although the high percentage of LAGBs in the AM ODS CrCoNi may have a negative impact on its creep resistance, the large number of vertical GBs provides a slight positive resistance to the propagation of strain across grains.
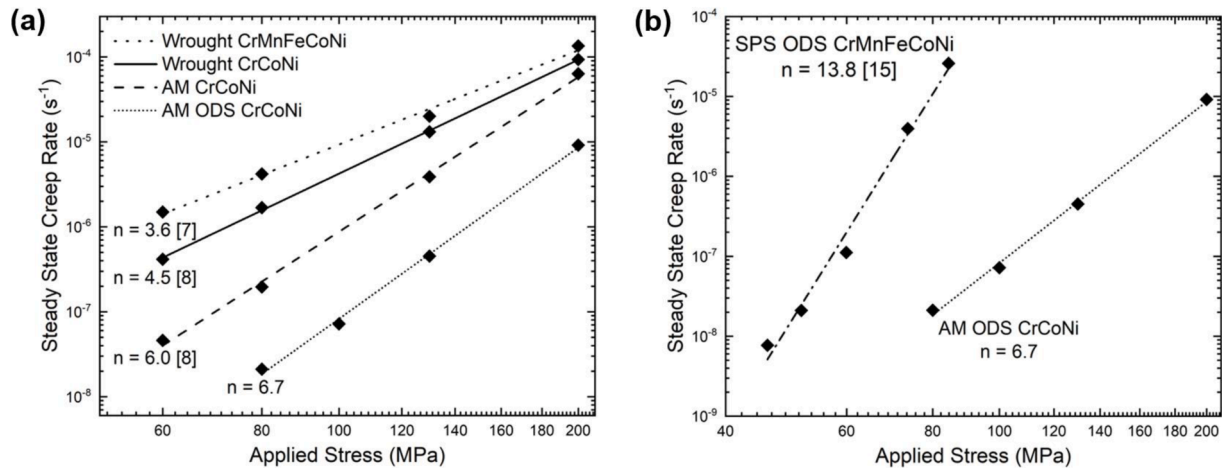
Fig. 6. Log-log plot of steady state creep rate vs applied stress for (a) wrought Cantor alloy [7], wrought CrCoNi [8], AM CrCoNi [8], and AM ODS CrCoNi at 1023 K and (b) SPS ODS Cantor alloy [15] and AM ODS CrCoNi at 1023 K.
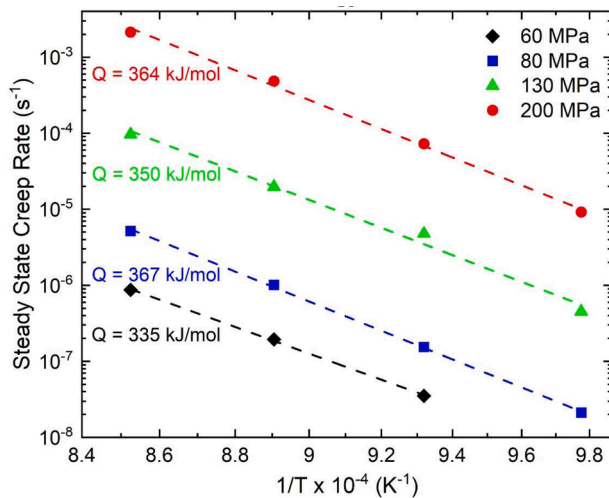

Fig. 7. Semi-log plot of state creep rate vs 1/T for AM ODS CrCoNi.

One factor that may impact the above interpretation is the occurrence of dynamic recrystallization (DRX) at the highest creep rates. However, mechanically, none of the strain-time creep curves for AM CrCoNi or AM ODS CrCoNi exhibited the characteristic strain oscillations that are commonly observed when dynamic recrystallization occurs during a creep experiment. Furthermore, the stress exponents for the two materials are not significantly different. The strain-time curves and similar stress exponents suggest that dynamic recrystallization does not affect the measured results.

Microstructurally, the AM ODS CrCoNi specimen tested at 1123 K and 200 MPa (one of the short tests with a high strain rate) did not exhibit evidence of significant dynamic recrystallization. A figure showing an EBSD map, a GB misorientation map, and an IPF contour plot is presented in Fig. S3. The grains remain elongated after testing with a grain size of 22.6 ± 3.5 µm in the Z-direction of the YZ plane and 7.4 ± 2.4 µm in the Y-direction of the YZ plane. These dimensions are statistically indistinguishable from those of the undeformed material. Some equiaxed grains are observed in the deformed material as is the case in the undeformed material. Additionally, it was observed that the percentage of LAGB is slightly lower (44.7%) and the percentage of HAGB is slightly higher (48.9%) in the specimen crept at 1123 K and 200 MPa. A slight change in texture between the undeformed and deformed material was observed, resulting in a Taylor factor of 3.17 in the deformed material compared to the Taylor factor of 3.39 in the

undeformed material. These results suggest that any dynamic recrystallization that occurred was limited in extent.

These mechanical and microstructural results indicate that dynamic recrystallization may have occurred to a small extent but did not significantly influence the measured creep results.

3.3. Characterization of dislocation structure and oxides in AM ODS CrCoNi

The AM ODS CrCoNi in the HIPed, annealed, and crept condition was examined by TEM to understand the evolution of the dislocation structure in this material and characterize the oxides present and their interactions with dislocations. The dislocation structure of the HIPed condition is illustrated in Fig. 8, showing a moderate dislocation density, dislocation/oxide interactions, extended nodes, and stacking fault tetrahedra (SFT). Extended nodes are a low energy dislocation configuration and are present in this alloy due to its low stacking fault energy of 22 ± 4 mJ m^{-2} [34]. SFT form as a result of vacancy condensation, which is a process that is assisted by low stacking fault energy. Silcox and Hirsch first observed SFT in quenched gold [35]. The SFT in the AM material likely formed during the rapid cooling associated with the L-PBF process which occurs at rates that are similar to or higher than quenching.

The dislocation structure of AM ODS CrCoNi after annealing at 1023 K for 3.5 h is observed in Fig. 9. This annealing temperature and time were chosen to imitate the process that takes place before creep testing in which the furnace temperature is allowed to equilibrate, leading to changes in dislocation structure immediately before the start of the test. STEM-EDS of the annealed material revealed yttrium and chromium rich oxides as seen in Fig. 10. The latter were also observed in the non-ODS CrCoNi [8]. Annealing the AM ODS CrCoNi resulted in the reduction of stored energy via dislocation network formation since dislocations were pinned at yttria particles and unable to move to annihilate with dislocations of the opposite sign. This mechanism of reducing stored energy during annealing is unlike that of the non-ODS CrCoNi in which dislocations are able to annihilate, leading to a very low dislocation density at the start of the creep tests [8]. Dislocation/oxide interactions, extended nodes, and SFT are present in the annealed material with SFT being more prevalent than in the HIPed material. Fig. S4 shows additional STEM-EDS of the annealed material illustrating dislocations that are pinned by yttria.

The dislocation structure of AM ODS CrCoNi at steady state for a temperature of 1023 K and a stress of 80 MPa is shown in Fig. 11 and displays a high dislocation density. Long arrays of relatively straight dislocations are observed in the crept material, which is significantly
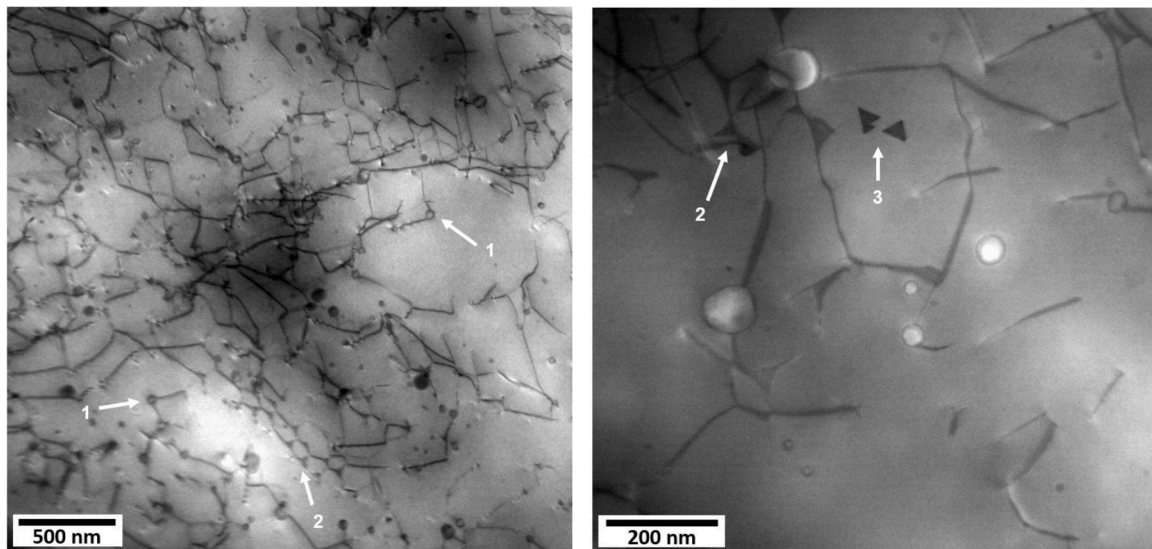
Fig. 8. Dislocation structure of HIPed CrCoNi showing dislocation/oxide interactions (arrows 1), extended nodes (arrows 2), and SFT (arrow 3).
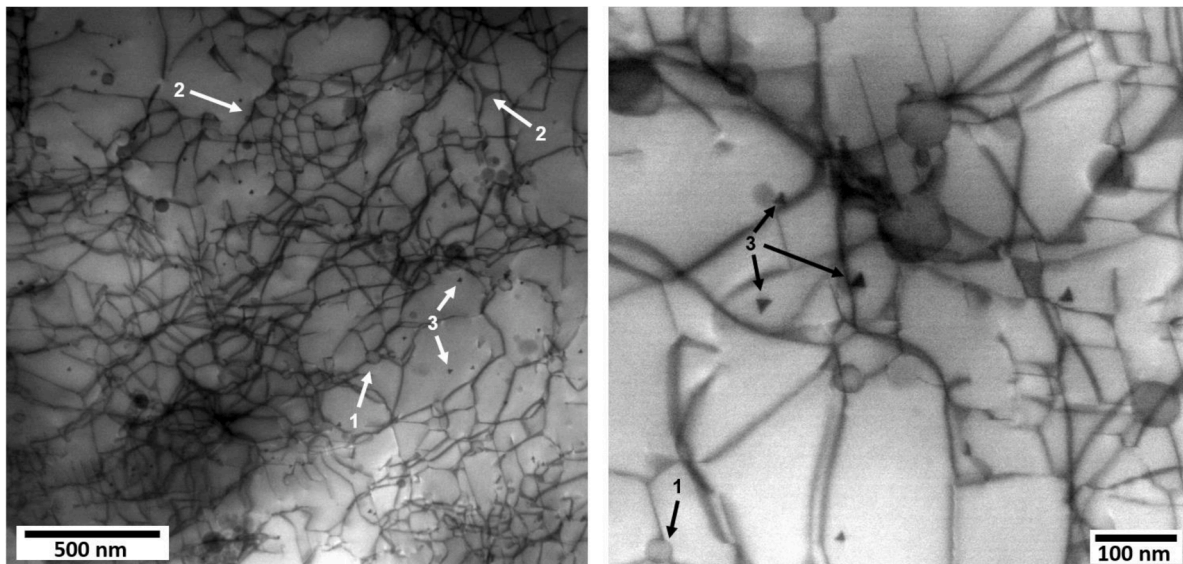

Fig. 9. Dislocation structure of annealed CrCoNi showing dislocation/oxide interactions (arrows 1), extended nodes (arrows 2), and SFT (arrows 3).

different from the lower density of individual curved dislocations observed in non-ODS CrCoNi [8]. The presence of dislocation arrays that are perpendicular suggests that they may represent incipient subgrain formation. STEM-EDS of the specimen crept to steady state at 1023 K and 80 MPa, as seen in Fig. 12, illustrates dislocation interactions with an yttria particle. To determine the character of dislocations interacting with oxides, $g \bullet b$ analysis was implemented as illustrated in Fig. S5. Dislocation/oxide interactions were imaged from seven different g vectors. Burgers vectors resulting in $g \bullet b = 0$ for g vectors in which dislocations were not visible were projected onto the TEM images to determine if the dislocation line vectors and Burgers vectors were parallel (screw dislocation), perpendicular (edge dislocation), or at an intermediate angle (mixed dislocation). The character of these dislocations is mixed necessitating that they interact with and climb over oxides rather than cross slipping to another glide plane.

3.4. Post creep fracture characteristics of AM ODS CrCoNi

The creep ductilities of AM ODS CrCoNi over the range of tested applied stresses are shown in Fig. 13. The overall average creep ductility of this material was found to be $11.1 \pm 5.0\%$. The large standard deviation associated with this creep ductility stems from a significantly greater value at an applied stress of 200 MPa, shown in Fig. 13. For tests at 130 MPa and lower, the average creep ductility is $8.5 \pm 2.0\%$ which is slightly higher than the average creep ductility reported for the non-ODS material ($7.1 \pm 1.2\%$) tested in the same range of applied stress and temperature [8]. For comparison, the creep ductilities of wrought CrCoNi and Cantor alloy have been reported as $17.6 \pm 1.6\%$ and $30.7 \pm 2.6\%$, respectively [7,8], which reveals that the AM process decreases creep ductility.

Creep ductility is generally related to stress concentrations on GB triple points due to GB sliding, dislocation pile-ups against GBs (Zener-Stroh mechanism), and hard particles on GBs that lead to the nucleation of voids which coalesce and result in intergranular fracture [36–40]. The
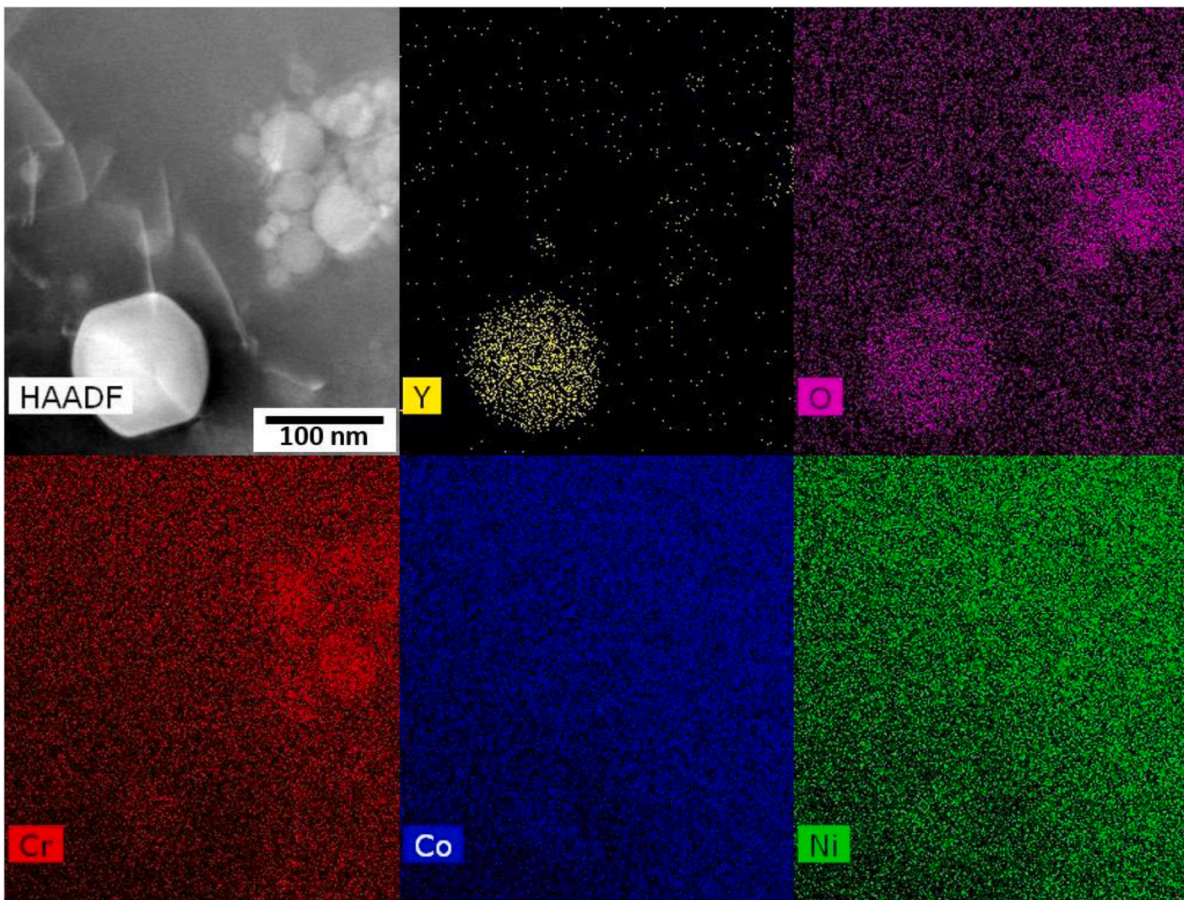
Fig. 10. High angle annular dark field (HAADF) and STEM-EDS of annealed AM ODS CrCoNi revealing yttrium and chromium rich oxides.
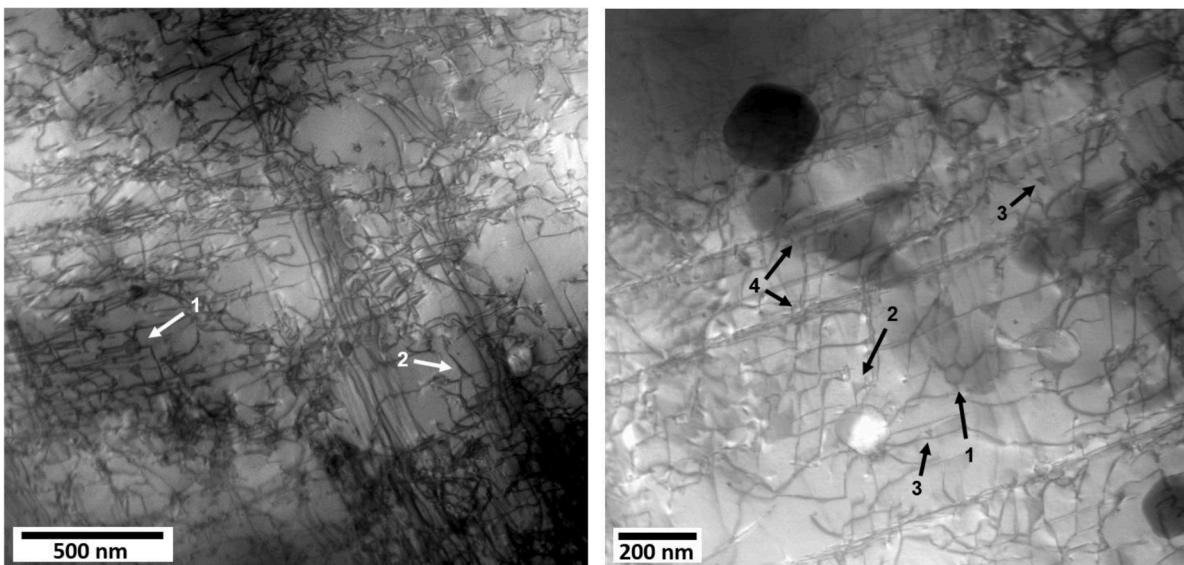

Fig. 11. Dislocation structure of AM ODS CrCoNi crept to steady state at 1023 K and 80 MPa showing dislocation/oxide interactions (arrows 1), extended nodes (arrows 2), SFT (arrows 3), and slip traces (arrows 4).

fracture surface of AM ODS CrCoNi is shown in Fig. 14 illustrating the cavities that have nucleated around oxides. The addition of yttria in the AM ODS CrCoNi provides a larger number of hard particles in this material compared to its non-ODS counterpart leading to the expectation that its creep ductility will be lower. This interpretation is supported by a study conducted by Dyson demonstrating that creep ductility

decreases as the rate of cavity production increases [41]. However, non-ODS AM CrCoNi has a lower creep ductility than AM ODS CrCoNi [8]. Thus, the higher creep ductility of the AM ODS material can be attributed to the higher percentage of LAGBs that enable easy propagation of deformation across grains and the elongated grains along the loading direction. The higher percentage of LAGBs in the AM ODS
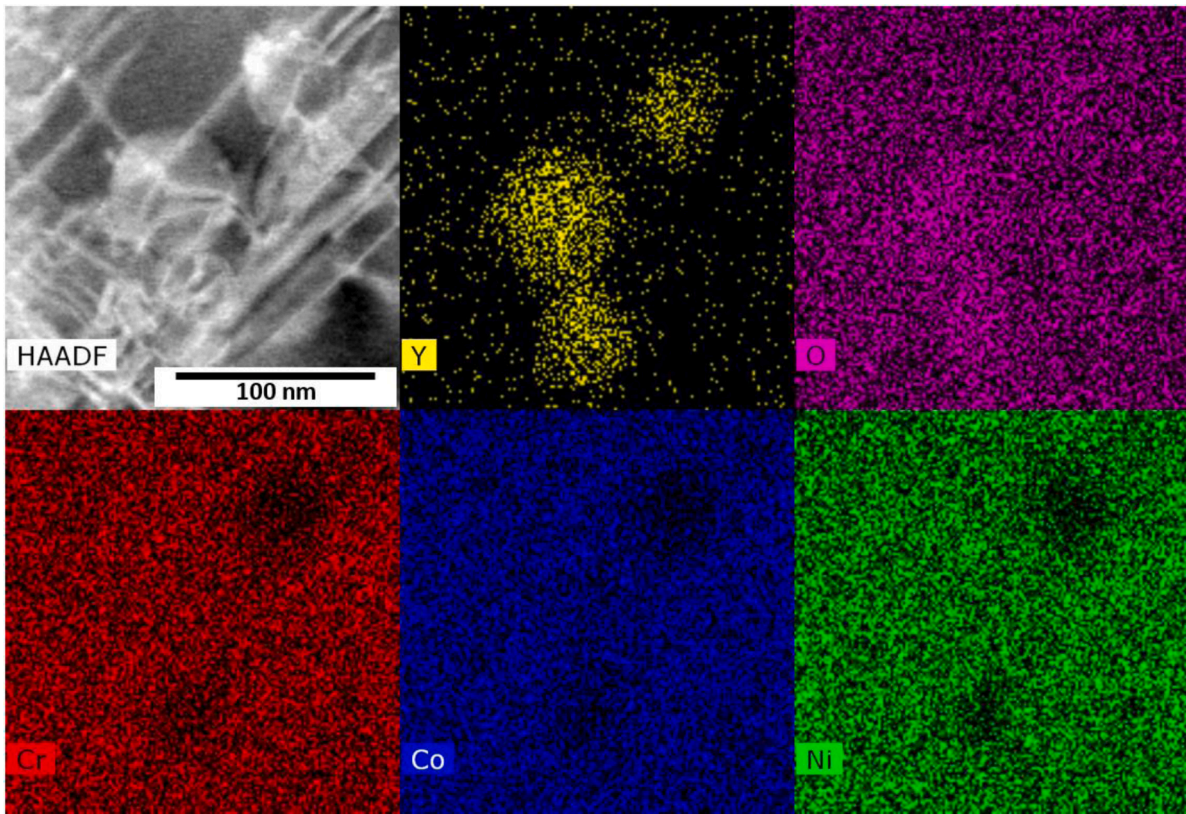
Fig. 12. HAADF and STEM-EDS of AM ODS CrCoNi crept to steady state at 1023 K and 80 MPa illustrating dislocation/oxide interactions.
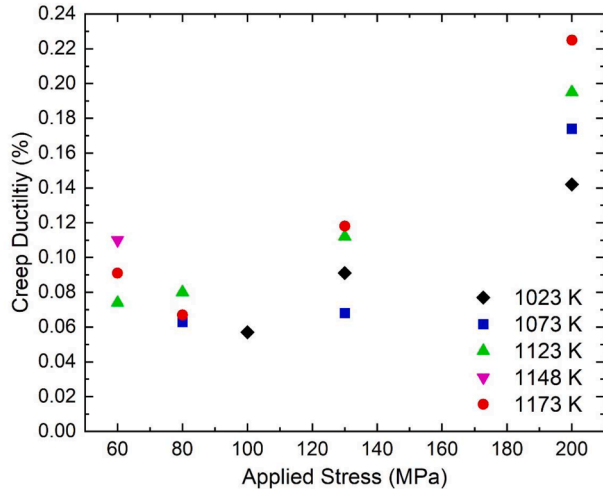

Fig. 13. Plot illustrating creep ductility of AM ODS CrCoNi showing an increase at an applied stress of 200 MPa.

Fig. 14. Fracture surfaces of AM ODS CrCoNi following creep rupture at 1023 K and 130 MPa.

material reduces the prevalence of the Zener-Stroh mechanism compared to the non-ODS material. Since dislocation pile-ups are more likely to propagate deformation through LAGBs, Zener-Stroh induced cavities are less likely to nucleate in the ODS material. Additionally, the elongated grain structure resulted in fewer adjacent transverse grain boundaries making the propagation of transverse cracks more difficult. This effect can be observed in Fig. 15, which shows the surface of a fractured AM ODS CrCoNi specimen and illustrates the presence of a highly tortuous intergranular crack path.
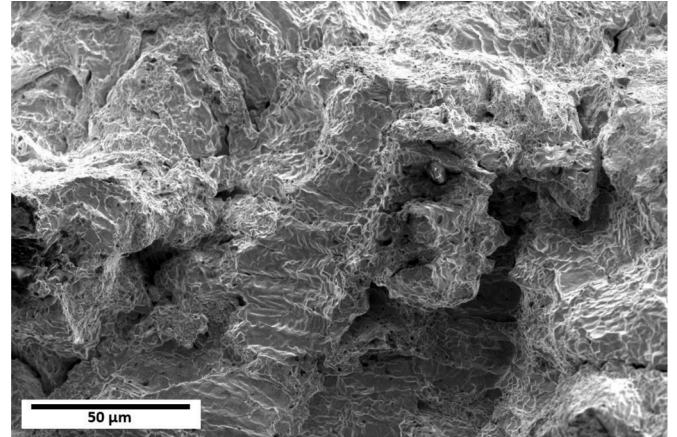
4. Conclusions

Constant stress creep tests in the ranges of 1023–1173 K and 60–200 MPa were conducted on an additively manufactured (AM) oxide dispersion strengthened (ODS) CrCoNi multi-principal element alloy to determine its creep behavior. SEM and TEM were used to observe the initial microstructure and dislocation structure, steady state dislocation structure, and fracture surface after rupture to understand the underlying creep deformation mechanisms of this material.

1. A stress exponent of 6.5 ± 0.1 and activation energies in the range of 335–367 kJ/mol were measured. This stress exponent is below the value of 10 or greater normally associated with ODS materials
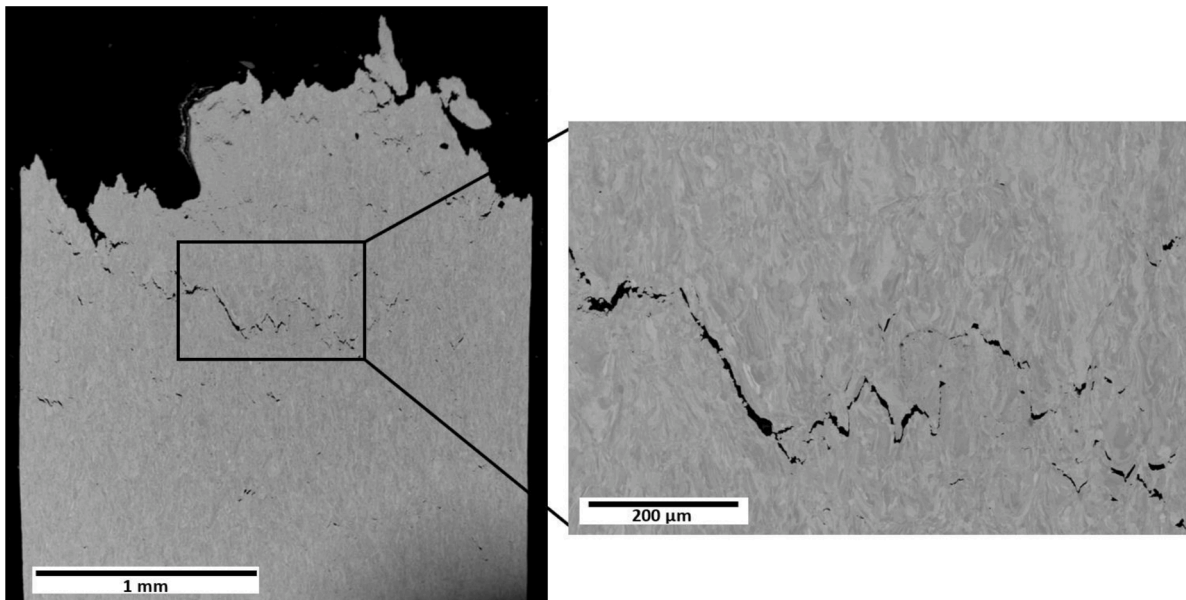
Fig. 15. Surface of AM ODS CrCoNi specimen following creep rupture at 1123 K and 80 MPa.

suggesting the 0.6 vol% of yttria is most likely too low to cause significant dislocation/oxide interactions typical of ODS materials. However, the AM ODS CrCoNi did exhibit an 84% lower steady state creep rate than its non-ODS counterpart at similar stresses and temperatures.

2. The average creep ductility of tests with an applied stress of less than 130 MPa was 8.5 ± 2.0%. Creep ductility is significantly greater at an applied stress of 200 MPa. The yttria and Cr-rich oxides act as cavity nucleation sites leading to void coalescence which is expected to decrease creep ductility while the high percentage of LAGBs allow easy propagation of deformation across grain boundaries avoiding the Zener-Stroh mechanism of cavity formation, which should increase creep ductility. The dynamic balance of these two mechanisms appears to favor the easy propagation of slip across LAGBs at the highest applied stress leading to higher ductility.

3. The steady state dislocation structure of AM ODS CrCoNi consists of long arrays of relatively straight dislocations with numerous dislocation/oxide interactions, extended nodes, and SFT. This dislocation structure is significantly different than its non-ODS counterpart which exhibits individual curved dislocations with dislocation multijunctions and jogs.

Declaration of competing interest

The authors declare that they have no known competing financial interests or personal relationships that could have appeared to influence the work reported in this paper.

Acknowledgements

Supplementary materials

Supplementary material associated with this article can be found, in the online version, at doi:10.1016/j.actamat.2023.119032.

References

[1] F. Otto, A. Dlouhy, C. Somsen, H. Bei, G. Eggeler, E.P. George, The influences of temperature and microstructure on the tensile properties of a CoCrFeMnNi high-entropy alloy, Acta Mater. 61 (2013) 5743–5755.

[2] B. Gludovatz, A. Hohenwarter, K.V.S. Thurston, H. Bei, Z. Wu, E.P. George, R.O. Ritchie, Exceptional damage-tolerance of a medium-entropy alloy CrCoNi at cryogenic temperatures, Nat. Commun. 7 (2016).

[3] G. Laplanche, A. Kostka, O.M. Horst, G. Eggeler, E.P. George, Microstructure evolution and critical stress for twinning in the CrMnFeCoNi high-entropy alloy, Acta Mater. 118 (2016) 152–163.

[4] J. Miao, C.E. Slone, T.M. Smith, C. Niu, H. Bei, M. Ghazisaeidi, G.M. Pharr, M. MJ, The evolution of the deformation substructure in a Ni-Co-Cr equiatomic solid solution alloy, Acta Mater. 132 (2017) 35–48.

[5] F.D.G. Filho, R.O. Ritchie, M.A. Meyers, M. SN, Cantor-derived medium-entropy alloys: bridging the gap between traditional metallic and high-entropy alloys, J. Mater. Res. Technol. 17 (2022) 1868–1895.

[6] Z. Wu, H. Bei, G.M. Pharr, E.P. George, Recovery, recrystallization, grain growth and phase stability of a family of FCC-structured multi-component equiatomic solid solution alloys, Intermetallics 46 (2014) 131–140.

[7] M. Zhang, E.P. George, J.C. Gibeling, Tensile creep properties of a CrMnFeCoNi high-entropy alloy, Scr. Mater. 194 (2021).

[8] G. Sahragard-Monfared, M. Zhang, T.M. Smith, A.M. Minor, E.P. George, J.C. Gibeling, The influence of processing methods on creep of wrought and additively manufactured CrCoNi multi-principal element alloys, submitted to Acta Materialia.

[9] J.Y. He, H. Wang, H.L. Huang, X.D. Xu, M.W. Chen, Y. Wu, X.J. Liu, T.G. Nieh, K. An, Z.P. Lu, A precipitation-hardened high-entropy alloy with outstanding tensile properties, Acta Mater. 102 (2016) 187–196.

[10] H. Shahmir, M. Nili-Ahmadabadi, A. Shafiee, T.G. Langdon, Effect of a minor titanium addition on the superplastic properties of a CoCrFeNiMn high-entropy alloy processed by high-pressure torsion, Mater. Sci. Eng. A 718 (2018) 468–476.

[11] Z. Fu, L. Jiang, J.L. Wardini, B. MacDonald, H. Wen, W. Xiong, D. Zhang, Y. Zhou, T.J. Rupert, W. Chen, E.J. Lavernia, A high-entropy alloy with hierarchical nanoprecipitates and ultrahigh strength, Sci. Adv. 4 (2018).

[12] A. Hoffman, L. He, M. Luebbe, H. Pommerenke, J. Duan, P. Cao, K. Sridharan, Z. Lu, H. Wen, Effects of Al and Ti additions on irradiation behavior of FeMnNiCr multi-principal-element alloy, JOM 72 (2020) 150–159.

[13] D.A. Santana, K.R. Santos, C.S. Kiminami, F.G. Coury, Design, phase equilibria, and coarsening kinetics of a new γ/γ' precipitation-hardened multi-principal element alloy, J. Alloys Compd. 882 (2021).

[14] H. Hadraba, Z. Chlup, A. Dlouhy, F. Dobes, P. Roupcova, M. Vilemova, J. Matejicek, Oxide dispersion strengthened CoCrFeNiMn high-entropy alloy, Mater. Sci. Eng. A 689 (2017) 252–256.

[15] F. Dobes, H. Hadraba, Z. Chlup, A. Dlouhy, M. Vilemova, J. Matejicek, Compressive creep behavior of an oxide-dispersion-strengthened CoCrFeMnNi high-entropy alloy, Mat. Sci. Eng. a-Struct. 732 (2018) 99–104.

[16] T.M. Smith, A.C. Thompson, T.P. Gabb, C.L. Bowman, C.A. Kantzos, Efficient production of a high-performance dispersion strengthened, multi-principal element alloy, Sci. Rep. (2020).

[17] D. Yang, Y. Liu, N. Qu, T. Han, M. Liao, Z. Lai, J. Zhu, Effect of fabrication methods on microstructures, mechanical properties and strengthening mechanisms of Fe0.25CrNiAl medium-entropy alloy, J. Alloys Compd. 888 (2021).

[18] O.N. Senkov, D.B. Miracle, K.J. Chaput, J. Couzinie, Development and exploration of refractory high entropy alloys—a review, J. Mater. Res. 33 (19) (2018) 3092–3128.

[19] C. Liu, C. Gadelmeier, S. Lu, J. Yeh, H. Yen, S. Gorsse, U. Glatzel, A. Yeh, Tensile creep behavior of HfNbTaTiZr refractory high entropy alloy at elevated temperatures, Acta Mater. 237 (2022).

[20] C. Gadelmeier, Y. Yang, U. Glatzel, E.P. George, Creep strength of refractory high-entropy alloy TiZrHfNbTa and comparison with Ni-base superalloy CMSX-4, Cell Rep. Phys. Sci. 3 (8) (2022).

[21] P. Kumar, S.J. Kim, Q. Yu, J. Ell, M. Zhang, Y. Yang, J.Y. Kim, H.-K. Park, A.M. Minor, E.S. Park, R.O. Ritchie, Compressive vs. tensile yield and fracture toughness behavior of a body-centered cubic refractory high-entropy superalloy Al0.5Nb1.25Ta1.25TiZr at temperatures from ambient to 1200°C, Acta Mater. 245 (2023).

[22] S.E. Broyles, M. Zhang, J.C. Gibeling, Influence of annealing on the creep behavior of GlidCop Al-15, Mater. Sci. Eng. A 779 (2020).

[23] M.W. Decker, J.R. Groza, J.C. Gibeling, Creep properties of an extruded copper-8% chromium-4% niobium alloy, Mat. Sci. Eng. a-Struct. 369 (1–2) (2004) 101–111.

[24] C.E. Slone, J. Miao, E.P. George, M.J. Mills, Achieving ultra-high strength and ductility in equiatomic CrCoNi with partially recrystallized microstructures, Acta Mater. 165 (15) (2019) 496–507.

[25] S. Liu, D. Wan, S. Guan, Y. Fu, X. Ren, Z. Zhang, J. He, Microstructure and nanomechanical behavior of an additively manufactured (CrCoNiFe)94Ti2Al4 high-entropy alloy, Mater. Sci. Eng. A 823 (17) (2021).

[26] G.D. Sathiaraj, W. Skrotzki, A. Pukenas, R. Schaarschuch, R.J. Immanuel, S.K. Panigrahl, J.A. Chelvan, S.S.S. Kumar, Effect of annealing on the microstructure and texture of cold rolled CrCoNi medium-entropy alloy, Intermetallics 101 (2018) 87–98.

[27] M. Schneider, E.P. George, T.J. Manescau, T. Zalezak, J. Hunfeld, A. Dlouhy, G. Eggeler, G. Laplanche, Analysis of strengthening due to grain boundaries and annealing twin boundaries in the CrCoNi medium-entropy alloy, Int. J. Plastic. 124 (2020) 155–169.

[28] O.D. Sherby, P.M. Burke, Mechanical behavior of crystalline solids at elevated temperature, Prog. Mater. Sci. 13 (1968) 323–390.

[29] V.C. Nardone, J.K. Tien, On the creep rate stress dependence of particle strengthened alloys, Scripta Metallurg. 20 (1986) 797–802.

[30] S.E. Broyles, K.R. Anderson, J.R. Groza, J.C. Gibeling, Creep deformation of dispersion-strengthened copper, Metallurg. Mater. Trans. A 27 (1996) 1217–1227.

[31] R.W. Lund, W.D. Nix, High temperature creep of Ni-20Cr-2ThO2 single crystals, Acta Metallurg. 24 (5) (1976) 469–481.

[32] S. Chen, Q. Yu, The role of low angle grain boundary in deformation of titanium and its size effect, Scr. Mater. 163 (2019) 148–151.

[33] F. Habiyaremye, A. Guitton, F. Schafer, F. Scholz, M. Schneider, J. Frenzel, G. Laplanche, N. Maloufi, Plasticity induced by nanoindentation in a CrCoNi medium-entropy alloy studied by accurate electron channeling contrast imaging revealing dislocation-low angle grain boundary interactions, Mater. Sci. Eng. A 817 (2021).

[34] G. Laplanche, A. Kostka, C. Reinhart, J. Hunfeld, G. Eggele, E.P. George, Reasons for the superior mechanical properties of medium-entropy CrCoNi compared to high-entropy CrMnFeCoNi, Acta Mater. 128 (2017) 292–303.

[35] J. Silcox, P.B. Hirsch, Direct observations of defects in quenched gold, Philos. Mag. 4 (37) (1959) 72–89.

[36] F.A. McClintok, A criterion for ductile fracture by the growth of holes, J. Appl. Mech. 35 (2) (1968) 363–371.

[37] R. Lombard, H. Vehoff, Nucleation and growth of cavities at defined grain boundaries in bicrystals, Scripta Metallurg. 24 (3) (1990) 581–586.

[38] E.P. George, R.L. Kennedy, D.P. Pope, Review of trace element effects on high-temperature fracture of Fe- and Ni-base alloys, Physica Status Solidi A 167 (2) (1998) 313–333.

[39] Y.S. Lee, J. Yu, Effect of matrix hardness on the creep properties of a 12CrMoVNb steel, Mater. Trans. A 30A (1999) 2331–2339.

[40] M.E. Kassner, T.A. Hayes, Creep cavitation in metals, Int. J. Plastic. 19 (10) (2003) 1715–1748.

[41] B.F. Dyson, Continuous cavity nucleation and creep fracture, Scripta Metallurg. 17 (1) (1983) 31–37.